

A single-layer framework of variational tensor network states

Hongyu Chen,¹ Yangfeng Fu,¹ Weiqiang Yu,^{1,2} Rong Yu,^{1,2} and Z. Y. Xie^{1,2,*}

¹*School of Physics, Renmin University of China, Beijing 100872, China*

²*Key Laboratory of Quantum State Construction and Manipulation (Ministry of Education), Renmin University of China, Beijing, 100872, China*

We propose a single-layer tensor network framework for the variational determination of ground states in two-dimensional quantum lattice models. By combining the nested tensor network method [Phys. Rev. B **96**, 045128 (2017)] with the automatic differentiation technique, our approach can reduce the computational cost by three orders of magnitude in bond dimension, and therefore enables highly efficient variational ground-state calculations. We demonstrate the capability of this framework through two quantum spin models: the antiferromagnetic Heisenberg model on a square lattice and the frustrated Shastry-Sutherland model. Even without GPU acceleration or symmetry implementation, we have achieved the bond dimension of 9 and obtained accurate ground-state energy and consistent order parameters compared to prior studies. In particular, we confirm the existence of an intermediate empty-plaquette valence bond solid ground state in the Shastry-Sutherland model. We have further discussed the convergence of the algorithm and its potential improvements. Our work provides a promising route for large-scale tensor network calculations of two-dimensional quantum systems.

I. INTRODUCTION

Two-dimensional (2D) strongly correlated systems, such as interacting fermionic systems and frustrated quantum magnets, pose significant challenges for theoretical studies. Consequently, developing efficient and accurate numerical methods for these models constitutes a crucial branch of theoretical condensed matter physics. In recent decades, tensor network methods^{6,7} have attracted increasing attention. By combining the tensor-network ansatz^{1,2} stemming from the quantum entanglement, the contraction strategy originating from renormalization group^{3,4}, and modern optimization techniques developed in artificial intelligence⁵, tensor network methods have been successfully applied to diverse phenomena, including quantum magnetism^{8–11}, superconductivity^{12–14}, topological order^{15,16}, and quantum field theory^{17,18}.

For studying ground states of 2D quantum systems using tensor networks, three strategies are commonly adopted. The first maps the 2D quantum model to a three-dimensional classical one¹⁹, converting the quantum expectation value calculation into a statistical physics problem²⁰. The second employs imaginary-time evolution with wave function update schemes^{21–24} to obtain the ground state $|\Psi_g\rangle$ in the tensor-network representation, and then evaluate the expectation value $\langle \hat{O} \rangle$ of the operator \hat{O} by contracting the related tensor networks. The third one is the straightforward variational minimization: Starting from an arbitrary tensor network state $|\Psi\rangle$, the ground state of the system $|\Psi_g\rangle$ and its energy E_g are obtained by minimizing the energy estimator

$$E = \frac{\langle \Psi | \hat{H} | \Psi \rangle}{\langle \Psi | \Psi \rangle} \quad (1)$$

with respect to tensor parameters¹. Recently, this approach has become increasingly popular due to the

advent of the automatic differentiation technique²⁵, which, as a mature and widely applied algorithm²⁶, can efficiently calculate the gradient $\frac{dE}{d|\Psi\rangle}$ ²⁹ and easily integrate with gradient-based optimization method⁵ via various open-source packages^{27,28}.

A central challenge in all three approaches is the contraction of tensor networks. Unfortunately, contracting a general tensor network in more than one dimension is a $\#P$ -complete hard problem³⁰ that cannot be performed exactly for an infinite system even with translational invariance. To this end, a series of approximation algorithms based on the renormalization group idea have been developed^{3,6}, among which the corner transfer-matrix renormalization group (CTMRG)^{14,31–33} has been widely used. In two dimensions, the cost of the CTMRG algorithm scales as D^{10} in memory and D^{12} in computation with the bond dimension D when no symmetry or partial matrix decomposition is employed. The cost is extremely high for variational calculations, which typically require hundreds of rounds of such contractions. The problem becomes even more serious for minimization with the automatic differentiation since it needs huge memory to store intermediate data for the gradient $(\frac{dE}{d|\Psi\rangle})$ calculation. This issue pose severe limitation for the bond dimension D in variational minimization employing automatic differentiation.

To overcome this limitation, here we propose a single-layer framework of variational tensor network state calculation that incorporates the nested tensor network (NTN) method³⁴. By reformulating the double-layer structures of numerator and denominator in Eq. (1) into nested single-layer structures, the NTN method reduces the memory and computation cost of tensor network contraction by two and three orders of D , respectively. This allows us to perform variational minimization with significantly larger bond dimension. Our proposal works as follows: For any given state $|\Psi\rangle$, we utilize the NTN

to calculate the energy defined in Eq. (1), then calculate the gradient $\frac{dE}{d|\Psi\rangle}$, and finally update the wave function $|\Psi\rangle$ using the gradient information as usual²⁹. This procedure can be iterated many times until the calculated energy converges.

We validate this method on two benchmark models defined on infinite 2D lattices: the $S = 1/2$ square-lattice antiferromagnetic Heisenberg model and the frustrated Shastry-Sutherland model. The former has an antiferromagnetically long-range ordered ground state³⁵, while the latter hosts a series of ground states when tuning the strength of spin frustration J/J' ^{10,36}. In both cases, with the help of NTN, we can efficiently reach $D = 9$ even without any GPU utilization or symmetry implementation, which is difficult in previous variational calculations^{10,11,29}. The obtained ground-state energy and order parameters are consistent with previous calculations, but with better convergence. In particular, we provide clear evidence for an empty-plaquette valence bond solid (VBS) phase in the ground-state phase diagram of the Shastry-Sutherland model.

The rest of the paper is organized as follows. In Sec. II we first briefly review of the automatic differentiation-assisted variational calculation of tensor network state and the NTN method, then introduce our single-layer framework. In Sec. III, we present the numerical results of the Heisenberg model and the Shastry-Sutherland model in detail. Finally, we summarize and conclude in Sec. IV.

II. METHOD

In this section, we first review the basics of automatic differentiation-assisted variational calculation of tensor network representation of the ground state²⁹, the underlying double-layer structure in Eq. (1), and the NTN method³⁴, then we introduce the single-layer framework by combining the two parts together.

A. Variational calculation assisted by automatic differentiation

For concreteness, we take the projected entangled pair state (PEPS) on a square lattice as an example to explain how to determine the ground state of a quantum spin system in the PEPS representation. Without loss of generality, suppose we have an infinite system hosting a 2×2 sublattice structure, then the infinite PEPS ansatz can be written as

$$|\Psi\rangle = \sum_{\{\sigma\}} \left[\text{Tr} \prod_i [A_{r_{1i}x_ic_{1i}z_i}^{(i)}[\sigma_{ia}] B_{x_ir_{3i}c_{2i}w_i}^{(i)}[\sigma_{ib}] C_{r_{2i}y_ic_{3i}}^{(i)}[\sigma_{ic}] F_{y_ir_{4i}w_ic_{4i}}^{(i)}[\sigma_{if}]] \right] \dots \sigma_{ia}\sigma_{ib}\sigma_{ic}\sigma_{if} \dots \rangle \quad (2)$$

where the superscript i denotes the unit cell index, and $A^{(i)}, B^{(i)}, C^{(i)}, F^{(i)}$ are the four distinct tensors defined in the i -th unit cell. Tr means summing over all the tensor subscripts that correspond to the link indices, and \sum means summation over all the physical spin configurations $\{\sigma\}$. A sketch of the $|\Psi\rangle$ is illustrated in Fig. 1.

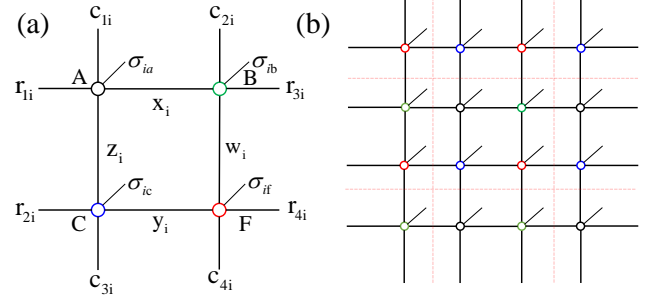


FIG. 1: An illustration of the infinite PEPS ansatz with a 2×2 sublattice, as expressed in Eq. (2). (a) A 2×2 unit cell. (b) Infinite PEPS wave function with translational invariance. Local tensors defined on the dots with the same color are identical. Dashed lines separate different unit cells.

According to Eq. (2), any quantum state $|\Psi\rangle$ satisfying the area law can be compatibly expressed as a superposition of spin configurations, where the coefficient of each term is represented as a tensor-network summation denoted by Tr . For an infinite system with translational symmetry, we assume the local tensors in different unit cells are the same, as illustrated in Fig. 1(b). Therefore, for any given local tensors, we can introduce a shorthand

$$X = [\vec{A}, \vec{B}, \vec{C}, \vec{F}] \quad (3)$$

where \vec{A} is the local tensor A reshaped as a vector residing in the (D^4d) -dimensional space, and so are \vec{B} , \vec{C} and \vec{F} . X is then a $(4D^4d)$ -dimensional vector storing all the variational parameters necessary to specify a quantum state $|\Psi(X)\rangle$ represented as Eq. (2). Here D is the bond dimension, which is the upper bound of all the subscripts appeared in Eq. (2), and d is the physical dimension for each σ . A tensor with a larger D contains more parameters, and is expected to have stronger representation power and better accuracy for a state. However, this also means heavier cost (discussed in Sec. II B). To find the PEPS representation of the ground state $|\Psi_g\rangle$ of a Hamiltonian system, we need to solve the following optimization problem

$$\arg \min_X E(X) \quad (4)$$

where $E(X)$ is determined by Eq. (1) but now its dependence of X is explicitly written.

In this work, we follow the variational minimization approach outlined in Sec. I. Starting from an initial

$|\Psi(X_0)\rangle$, we can use well-established techniques, such as the CTMRG^{14,31–33}, to compute the energy $E(X)$. In this procedure, when the automatic differentiation technique is used. Then, as long as E is obtained successfully, we can calculate the gradient $\frac{\partial E(X)}{\partial X}|_{X=X_0}$ conveniently by simply calling some open source packages, such as PyTorch²⁷ and Zygote²⁸, without any extra operation. After the gradient information is obtained, we can update X using classic optimization algorithms, such as L-BFGS⁵, to get a better trial X_1 and the corresponding wave function $|\Psi(X_1)\rangle$. Similarly, we can evaluate $E(X_1)$, calculate $\frac{\partial E(X)}{\partial X}|_{X=X_1}$, and then obtain a better X_2 and $|\Psi(X_2)\rangle$. This iteration can be repeated as many as we want until the gradient $\frac{\partial E(X)}{\partial X}$ is sufficiently small or the energy E converges within some tolerance. The converged X^* yields an approximate solution of Eq. (4) and thereby provides an approximate representation of $|\Psi_g\rangle$.

In essence, the reverse mode of automatic differentiation²⁵ uses the chain rule of derivative, usually referred to as backpropagation³⁷ in optimization engineering, to compute the gradient information. Formally, in this case

$$\frac{\partial E}{\partial X} = \frac{\partial E}{\partial T^{(n)}} \frac{\partial T^{(n)}}{\partial T^{(n-1)}} \frac{\partial T^{(n-1)}}{\partial T^{(n-2)}} \cdots \frac{\partial T^{(2)}}{\partial T^{(1)}} \frac{\partial T^{(1)}}{\partial X} \quad (5)$$

where the $\{T^{(i)}, i = 1, 2, \dots, n\}$ are the intermediate variables which are involved in the process of evaluating E , e.g., the temporal local tensors generated in the CTMRG iterations. We assume n related local tensors in Eq. (5) have been generated. In order to compute the gradient $\frac{\partial E}{\partial X}$, these intermediate tensors generally need to be stored in memory. In the tensor network framework, if the transformations involved in the energy-evaluating contraction algorithms are treated as independent parameters, the automatic differentiation is then equivalent to the backward iteration procedure of the second renormalization group method³⁸ for obtaining the global environment. Therefore, in this sense, this kind of variational tensor network approach tries to solve Eq. (4) by global optimization, and that is one of the reasons why this method can be successfully applied to study a series of strongly correlated systems²⁹, e.g., quantum spin-orbital liquid³⁹, altermagnetism¹¹, deconfined quantum critical point¹⁰, even with a small bond dimension.

B. Review of the NTN method

As mentioned in the last section, the intermediate local tensors $\{T^{(i)}\}$ in Eq. (5) have to be stored in memory before the gradient is obtained. This poses a great challenge for memory and strongly limits the bond dimension D in the calculations. To see this, in Fig. 2, we sketch $\langle\Psi|\Psi\rangle$ whose calculation cannot be avoided in evaluating Eq. (1). Conventionally, to calculate $\langle\Psi|\Psi\rangle$,

firstly one need to form a reduced tensor

$$T_{ii',jj',kk',ll'}^a \equiv \sum_{\sigma} A_{i,j,k,l}[\sigma] A_{i',j',k',l'}^*[\sigma] \quad (6)$$

as illustrated in Fig. 2(a). T^b , T^c , T^f can be defined similarly corresponding to the 2×2 unit cell in Fig. 1(a). Obviously, each local tensor T , and thus the resulting tensor network $\langle\Psi|\Psi\rangle$, has a *double-layer* structure. That is, if the representation $|\Psi\rangle$ in Eq. (2) has bond dimension D , then each index of T^a in Eq. (6) and the resulting $\langle\Psi|\Psi\rangle$ have bond dimension D^2 . Therefore, evaluating the energy $E(X)$ requires contracting a tensor network with bond dimension D^2 , which generally leads to a computational cost of about D^{12} ³⁴ when the CTMRG algorithm is employed^{40,41}. As explained in Sec. II A, the memory cost of storing all intermediate tensors generated in this procedure in automatic differentiation is typically D^8 , which would expold fast with increasing D . Therefore, the substantial memory and computational demands impose a stringent constraint on the practically attainable bond dimension D in automatic differentiation-based variational minimization.

In order to solve this problem, the NTN method regards $\langle\Psi|\Psi\rangle$ as a *single-layer* network with a nesting structure, as illustrated in Fig. 2(c). To be specific, instead of summing over the physical index σ and forming a reduced tensor T^a , as done in Eq. (6), NTN considers the physical indices $\{\sigma\}$ and the link indices equally by regarding $\{\sigma\}$ as special link indices connecting nearby conjugated tensors, e.g., A^* in $\langle\Psi|$ and A in $|\Psi\rangle$, as shown in Fig. 2(b). In graphic terms, bra state $\langle\Psi|$ (blue) and ket state $|\Psi\rangle$ (red) lie in the same layer and are connected by $\{\sigma\}$. In order to avoid longer-range links, a virtual tensor X , equal to the direct product of two δ functions, is defined at each crossing point where the virtual links in $\langle\Psi|$ and $|\Psi\rangle$ intersect. Furthermore, to make the resulting network a square lattice, we modify one set of X to Y by combining an X and a σ . Formally, as shown in Fig. 2(d), X and Y can be defined in the following

$$X_{i,j,k,l} = \delta_{ij}\delta_{kl}, \quad Y_{i\sigma,j,k,l\sigma'} = \delta_{ij}\delta_{kl}\delta_{\sigma\sigma'} \quad (7)$$

where δ is the Kronecker-delta function. Finally, the nesting structure of $\langle\Psi|\Psi\rangle$ is illustrated in Fig. 2(c) as a single-layer network. Any expectation value of a local operator, such as local terms in the numerator in Eq. (1), i.e., $\langle\Psi|H_{ij}|\Psi\rangle$ where H_{ij} is a bond Hamiltonian, can be represented similarly but with some impurity tensors.

Though the idea is simple, the NTN method has a significant advantage that the bond dimension of $\langle\Psi|\Psi\rangle$ is no more than Dd , where d is the physical dimension associated with each σ , instead of D^2 as in Fig. 2(a). Since the nesting structure is essentially a single-layer tensor network, widely used methods such as CTMRG can be employed to perform the contraction efficiently. For example, suppose the environment dimension used in CTMRG is of the same order as D^2 required by the reduced tensor network with bond dimension D^2 . In that

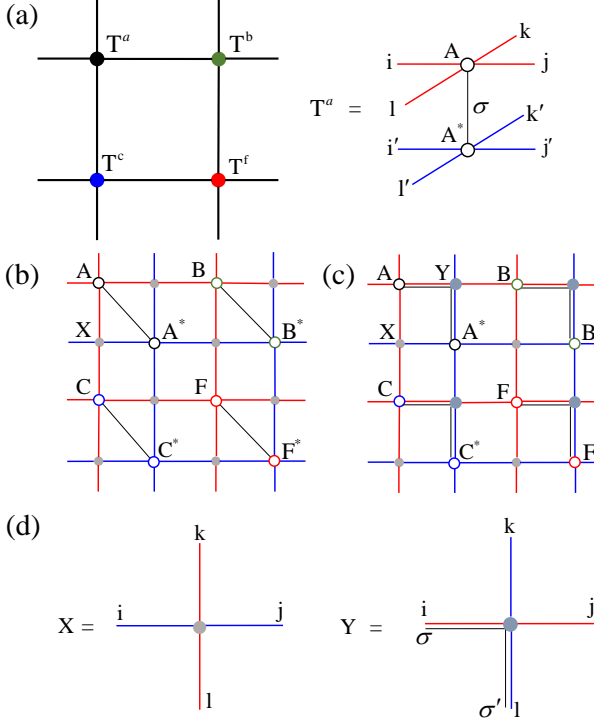


FIG. 2: An illustration of the NTN method. (a) The unit cell of the reduced network $\langle\Psi|\Psi\rangle$, corresponding to the unit cell of $|\Psi\rangle$ in Fig. 1. The double-layer structure of T is also shown, corresponding to Eq. (6). (b) The actual structure of (a), where $\langle\Psi|$ and $|\Psi\rangle$ are colored by blue and red, respectively. The slashed black lines denote physical indices $\{\sigma\}$. (c) The nested representation of (a) and (b) used in this work. Two additional tensors X and Y are introduced to form a compact single-layer tensor network. (d) The definition of X and Y , as expressed in Eq. (7).

case, ignoring the scaling of d , the contraction of this nested single-layer tensor network has a memory cost of about D^6 and a computational cost of about D^9 , which are much lower than those in the reduced method (D^8 and D^{12})³⁴.

Bearing this advantage, the NTN method has been used in a series of studies to extend D to larger values on the kagome lattice. For example, D was extended to 25 in Refs.^{8,34} to study the kagome spin liquid, also to 25 in Ref.⁴⁰ to study the kagome Heisenberg model with DM interactions, and to 15 in Ref.⁴¹ to study the kagome Heisenberg model with chiral interactions.

C. The single-layer framework of variational tensor network states

As far as we know, in previous studies, such as Refs.^{8,34,40,41} mentioned in Sec. II B, the NTN method was only utilized in either expectation value

calculation or updating the wave function in imaginary-time evolution, but was seldom utilized in the variational calculation of the ground state wave function as discussed in Sec. II A.

In this work, we propose to incorporate the NTN method into the variational solution of the minimization problem, i.e., Eq. (4). The overall framework is summarized in the following:

(i). Firstly, we need to prepare an initial PEPS $|\Psi(X_0)\rangle$ from which the optimization begins. Either an arbitrary state specified by a random X_0 (this work) or an approximate PEPS obtained by imaginary-time evolution²¹⁻²⁴ can be accepted.

(ii). Compute the energy $E(X_0)$ through Eq. (1), where either boundary matrix product state^{42,43} or CTMRG (this work) can be used to contract the single-layer tensor network $\langle\Psi(X_0)|\Psi(X_0)\rangle$ with nested structure explained in Sec. II B. In this step, one can use automatic differentiation software packages, such as PyTorch²⁷ and Zygote²⁸ (this work), to implement the contraction algorithm. Once $E(X_0)$ is obtained, the gradient $\frac{\partial E(X)}{\partial X}|_{X=X_0}$ can be evaluated through Eq. (5) efficiently and automatically.

(iii). Using the gradient information obtained in step (ii), we can employ the gradient-based optimization algorithm, such as Adam and L-BFGS⁵ (this work), to get X_1 , the following prediction of the solution of Eq. (4). Then update the parameter by setting $X_0 = X_1$ and obtain a new PEPS $|\Psi(X_0)\rangle$.

(iv). Repeat steps (ii) and (iii) until the energy E converges or the gradient stops decreasing. Finally, we regard the output X_1 as an approximate solution of Eq. (4) and $|\Psi(X_1)\rangle$ as an approximate ground state correspondingly.

It should be noted that, by converting the reduced the double-layer structure in Fig. 2(a) to the nested single-layer structure in Fig. 2(c), we have made an acceptable sacrifice to reduce the bond dimension D^2 to Dd : the size of the unit cell is doubled from 2×2 to 4×4 . Therefore, to contract the tensor network by CTMRG, e.g., one has to employ the multisite version of the algorithm adapted to the nested structure. The specific version of the CTMRG algorithm used in this work, for a 4×4 unit cell, is illustrated in Fig. 3, which is a simple variant of the algorithm proposed in Ref.¹⁴.

Specifically, suppose the distinct tensors in a unit cell are denoted as $\{T^{(i,j)}, i, j = 0, 1, 2, 3\}$, which are all rank-4 tensors with bond dimension D ⁴⁴. In the multisite CTMRG method, the environment of the tensor $T^{(i,j)}$ located at the i -th row and j -th column in the 4×4 unit cell is represented as $\{C^{(i,j;\alpha)}, E^{(i,j;\beta)}\}$, where α and β run from 1 to 4 and corresponds to the four corner and four edge tensors for each $T^{(i,j)}$, as illustrated in Fig. 3(a). Therefore, in this case we have 64 distinct corners and 64 edges in total, stored independently for each $T^{(i,j)}$ but updated in a correlated manner. For example, in Fig. 3(b) we explicitly show the recursive relations between the environments of $T^{(i,j)}$ and $T^{(i,j+1)}$,

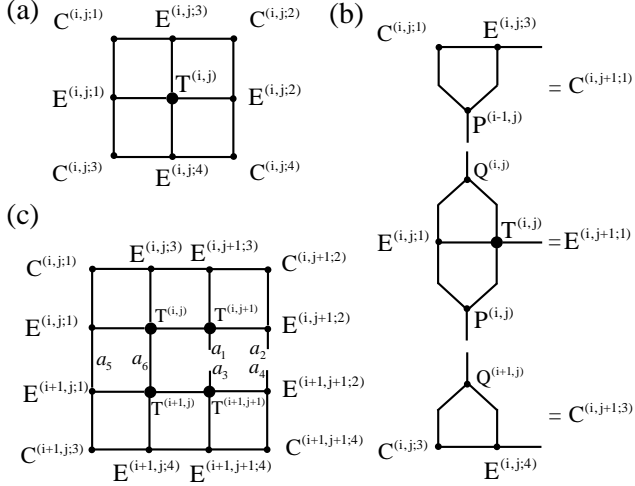


FIG. 3: A sketch of the CTMRG algorithm used in this work, for a tensor network with a 4×4 unit cell. The superscripts i and j should be taken modulo 4. (a) The environment of the local tensor located at the i -th row and j -th column in the unit cell. (b) The recursive relation between the environment of $T^{(i,j)}$ and $T^{(i+1,j)}$, in a left-move. (c) The 4×4 cluster used to determine the transformation matrices used in (b). Here $P^{(i,j)}$ and $Q^{(i+1,j)}$ will be determined, as expressed in Eqs. (8-9), and be inserted in the bonds denoted by a_5a_6 . The resulting framework constitutes an optimal approximation of the bond density matrix ρ , which has subscripts (a_1a_2, a_3a_4) .

which are used in a left-move step in the CTMRG iterations.

The core step of CTMRG is to find the transformation matrices $P^{(i,j)}$ and $Q^{(i,j)}$, which are of dimension $D\chi$ by χ . Here χ is the so-called environment dimension, which is the dimension of the bonds belonging only to the environment tensors. Following the bond density matrix approach developed in Refs. 14,20, we always use a 2×2 system surrounded by its environment to determine P and Q , as illustrated in Fig. 3(c), where the 4×4 block is intentionally split into two parts from right. Mathematically, $P^{(i,j)}$ and $Q^{(i+1,j)}$ are constructed in the following

$$P^{(i,j)} = R_s^t V \tilde{\Lambda}^{-1/2}, \quad Q^{(i+1,j)} = R_n^t U^* \tilde{\Lambda}^{-1/2} \quad (8)$$

where we have introduced the QR decomposition and singular value decomposition of two matrices N and S ,

$$N = Q_n R_n, \quad S = Q_s R_s, \quad R_n R_s^t = U \Lambda V^\dagger \quad (9)$$

Here the superscript t means matrix transpose. The $\tilde{\Lambda}$ in Eq. (8) is the truncated version (with dimension χ) of the full singular value matrix Λ in Eq. (9). N is the block tensor with subscripts (a_1a_2, a_5a_6) by contracting the eight tensors in the upper part of Fig. 3(c), and S is tensor with subscripts (a_3a_4, a_5a_6) by contracting

the lower part. It can be proved that by inserting the transformation matrices $P^{(i,j)}$ ($Q^{(i+1,j)}$) t in the bonds labeled by a_5a_6 between N and S in Fig. 3(c), the resulting network constitutes a truncated singular value decomposition of the bond density matrix $\rho_{a_1a_2, a_3a_4}$ which can be expressed as $\rho = NS^t$.

In a single step of left move, for a 4×4 unit cell, we need to determine four pairs of transformation matrices by performing Eqs. (8-9) for each i independently. And after that, one can use these transformations to update the related three environment tensors for each i by performing the contractions illustrated in Fig. 3(b). This finishes a single step of the left move. We need to perform such a step for each j , which means we have to perform four such steps in a single left move. Right, upward, and downward moves can be performed one by one similarly, and this completes a single CTMRG iteration. This iteration can be repeated once again, until all the spectra $\tilde{\Lambda}$ converge to some accepted accuracy.

From Fig. 3 and the analysis described above, it is easily shown that if the environment dimension χ is set to the order of D^2 empirically³⁴, and no symmetry or other advanced techniques like partial matrix decompositions are employed, then the above CTMRG algorithm utilized to contract a nested tensor network with bond dimension D has a memory cost about D^6 and a computational cost about D^9 ^{40,41}. This is more economical than the conventional reduced tensor network method as mentioned in Sec. II B and discussed in detail in Ref.³⁴. And this is the reason why we can extend our variational calculation equipped with automatic differentiation to $D = 9$ in this work.

III. RESULTS

In this section, we apply the single-layer variational tensor network framework, as explained in the last section, to two prototypical antiferromagnetic quantum spin-1/2 models. Even though neither spin symmetries, such as U(1) and SU(2), nor GPU hardware acceleration are utilized in this work, the ground-state energy and the order parameters characterizing the quantum phases are obtained accurately by pushing $D = 9$. This demonstrates the power of the proposed single-layer framework.

A. The Heisenberg model on a square lattice

The first model we studied is the antiferromagnetic spin-1/2 Heisenberg model on a square lattice, which was known to host a Néel antiferromagnetic ground state. To obtain such a state with a double sublattice structure, we use a compatible PEPS ansatz with 2×2 unit cell containing only two distinct local tensors, as shown in Fig. 4.

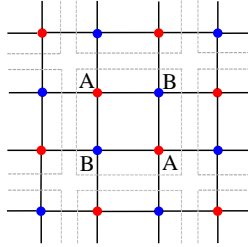


FIG. 4: The PEPS ansatz used in this work to study the square lattice Heisenberg model. Dashed lines separate the 2×2 unit cells.

The estimated ground-state energy is plotted in Fig. 5 as a function of D . It shows that the obtained energy systematically decreases as D increases, verifying the variational nature of the framework. When $D = 9$, we obtain an estimation about $E_g = -0.6693896$, which is already very close to the value $E_g = -0.6694421$ in quantum Monte Carlo simulation³⁵. If we make a further power-law fitting of $E_g(1/D)$, then in the large- D limit we obtain an extrapolation about $E_g = -0.66941$, which deviates from the quantum Monte Carlo estimation only by the order of 10^{-5} .

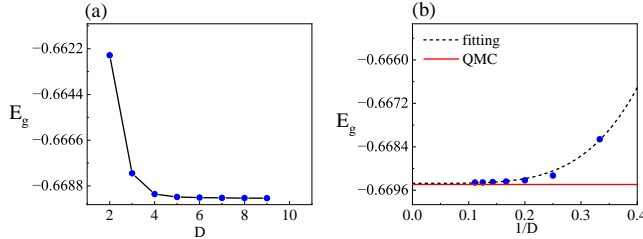


FIG. 5: The obtained ground-state energy E_g of the square lattice Heisenberg model. (a) E_g as a function of bond dimension D , with D ranging from 2 to 9. (b) A power-law fitting of data $E_g(1/D)$. The extrapolation to the large- D limit gives $E_g = -0.66941$. A quantum Monte Carlo estimation from Ref.³⁵, $E_g = -0.6694421$, is also shown as red solid.

As mentioned before, the ground state of this model is antiferromagnetically long-range ordered; therefore, we can use the magnetization M defined below as an order parameter to characterize the ground state,

$$M = \frac{1}{N} \sum_i |m_i|, \quad m_i = \left(\langle S_x^{(i)} \rangle, \langle S_y^{(i)} \rangle, \langle S_z^{(i)} \rangle \right) \quad (10)$$

where $S_\alpha^{(i)}$ is the α -component of the spin operator defined on the i -th inequivalent site in the unit cell, $|m_i|$ is the length of the magnetic vector m_i , and N is the total number of inequivalent sites in a unit cell. The obtained magnetization M as a function of D is plotted in Fig. 6. Similarly to E_g , the magnetization is also systematically lowered as D increases. When $D = 9$, M is lowered

to 0.31897, and the extrapolated value in the large- D limit obtained by a power fitting of the data $M(1/D)$ gives an estimation $M = 0.3159$, which is only slightly higher than the value $M = 0.307$ in quantum Monte Carlo simulation³⁵, but comparable to those from double-layer and variational update calculations^{29,45}. What's more, we find that the local magnetization m_i exhibits an explicit antiferromagnetic pattern indicated by staggered orientations. All these signatures are consistent with the Néel antiferromagnetic ground state.

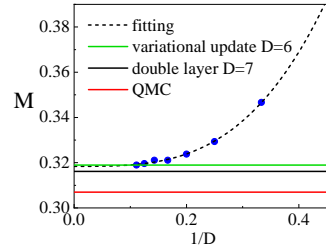


FIG. 6: The obtained magnetization M of the square lattice Heisenberg model. A power-law fitting of data (dashed line) gives $M = 0.3159$ in the large- D limit. The solid red line marks the value $M = 0.307$ from a quantum Monte Carlo estimation³⁵. The solid black and green lines mark the values of M from a $D = 7$ double layer²⁹ and a $D = 6$ variational update⁴⁵ tensor network calculations.

As described in Sec. II, there are two important hyperparameters in variational tensor network calculations. One is the bond dimension D of the PEPS ansatz as expressed in Eq. (2), the other is the environment dimension χ used in the CTMRG algorithms to evaluate $\langle \Psi | \Psi \rangle$ for a given D . Essentially, the calculation is variational with respect to D , but is not variational for χ . Therefore, for a given D , the expectation values $E(D)$ and $M(D)$ are reliable only under the condition that they are converged with respect to χ as χ increases³⁴. Therefore, in this work, in order to ensure the convergence of E and M for each D , we always keep the environment dimension χ sufficiently large. A detailed analysis for $D = 9$ is shown in Fig. 7. It shows that by increasing χ to 160, both the energy and the magnetization are systematically improved, and the convergence error is only about the order of 10^{-6} , which is already rather satisfactory for our purpose.

B. The frustrated Shastry-Sutherland model

The second model we focused on in this work is the spin-1/2 Shastry-Sutherland model defined by the following Hamiltonian

$$H = J \sum_{\langle i,j \rangle} \mathbf{S}_i \cdot \mathbf{S}_j + J' \sum_{\langle\langle i,j \rangle\rangle} \mathbf{S}_i \cdot \mathbf{S}_j, \quad J > 0, J' > 0 \quad (11)$$

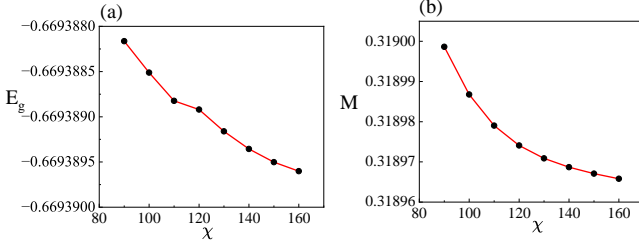


FIG. 7: Convergence analysis of E_g and M with respect to the environment dimension χ used in CTMRG, for the square lattice Heisenberg model with $D = 9$. (a) The ground-state energy E_g . (b) The magnetization M .

where \mathbf{S}_i is the three-component spin operator defined on i -the lattice point. A sketch of the Shastry-Sutherland lattice is illustrated in Fig. 8(a). From the view of the underlying square lattice, one can see that in Eq. (11), J denotes the nearest neighboring antiferromagnetic coupling, and J' denotes the next nearest neighboring coupling defined in only one set of squares and arranged as a wheelchair pattern. This model draws attentions in recent years^{10,36,46,47} because of the stabilization of a quantum disordered plaquette valence bond solid ground state in the intermediate J/J' regime of the phase diagram, as well as possible realization of a deconfined quantum critical point⁴⁸ and/or quantum spin liquid^{47,50,51} relevant to some interesting experimental results in real materials⁴⁹.

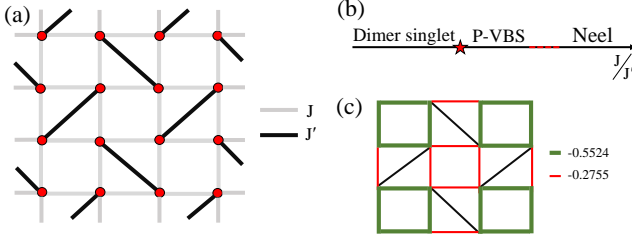


FIG. 8: The Shastry-Sutherland model we studied in this work, as expressed in Eq. (11). (a) The Shastry-Sutherland lattice. The grey bonds constitute the underlying square lattice, and the coupling strength on these bonds corresponds to J . The black bonds correspond to the coupling J' that forms a wheelchair pattern. (b) A sketch of the phase diagram consisting of a dimer singlet, a plaquette valence bond solid (VBS), and a Néel antiferromagnetic ground states with varying J/J' . The nature of the plaquette VBS to the antiferromagnetic transition is under debate, with the possibility of an intervening quantum spin liquid as marked by the red dashed region. (c) The bond correlation $\langle \mathbf{S}_i \cdot \mathbf{S}_j \rangle$ in the obtained ground state at $J/J' = 0.7$ in this work, consistent with the empty-plaquette VBS state¹⁰.

An illustration of the phase diagram is also shown in

Fig. 8(b). When J dominates, the ground state of this model is a Néel antiferromagnetic state, while when J' dominates, the two spins coupled by J' , as indicated by the black bonds in Fig. 8(a), forming a dimer singlet, and the ground state of the system is a direct product of these dimer singlets. In the intermediate regime, the ground state is a plaquette valence bond solid. However, there is much controversy on the competition between the full-plaquette and empty-plaquette VBS patterns^{10,36,49}, the nature of the phase transition between the Néel and VBS phases^{10,49}, and the possible existence of an intervening quantum spin liquid regime^{47,50,51}. In this work, using the proposed single-layer variational framework and setting $J' = 1$, we focus on two parameter settings: the possible VBS phase with $J = 0.7$, and the antiferromagnetic phase with $J = 0.8$.

In Fig. 9, we focus on $J = 0.7$, and plot the obtained ground-state energy E_g as a function of D . The variational feature remains pronounced, i.e., the energy systematically improves as D becomes larger. When $D = 9$, we have $E_g = -0.3880225$. If we fit the data $E_g(1/D)$ and extrapolate to the large- D limit, we obtain an estimation $E_g = -0.3885$ black dashed in Fig. 9(a)), which is consistent with the previous PEPS from finite systems⁴⁷. To make the result convincing, we analyze the energy for $D = 9$ with χ ranging from 90 to 140 in Fig. 9(b). It is clear that the energy has almost fully converged with a precision of about 10^{-6} .

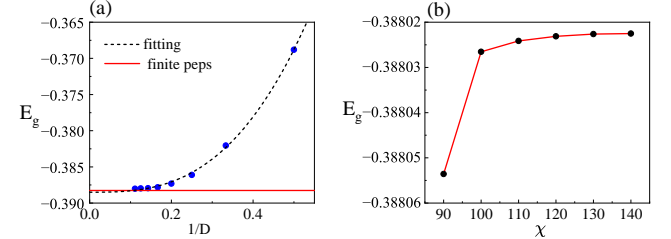


FIG. 9: The obtained ground-state energy E_g of the Shastry-Sutherland model at $J = 0.7$. (a) E_g as a function of bond dimension D , with D ranging from 2 to 9. A power-law fitting of data $E_g(1/D)$ is indicated by a black dashed line. For comparison, an extrapolation from finite PEPS calculations⁴⁷ is also plotted as a red solid line. (b) The convergence analysis of $E_g(\chi)$ for $D = 9$.

Further analysis shows that the obtained ground state is an empty-plaquette VBS state, which is illustrated in Fig. 8(c). To show this, firstly we introduce an order parameter M_p defined in the following

$$M_p = \frac{1}{4} \left| \sum_{\langle i,j \rangle \in \square} \langle \mathbf{S}_i \cdot \mathbf{S}_j \rangle - \sum_{\langle i,j \rangle \in \square} \langle \mathbf{S}_i \cdot \mathbf{S}_j \rangle \right| \quad (12)$$

where the two \sum sum over all the nearest neighbors in a single square without (\square) and with (\square) J' coupling, respectively. In Fig. 10(a), we plot the obtained M_p as a function of D . It shows clearly that the order

parameter converges gradually as D increases, and when $D = 9$ we obtain $M_p = 0.1384$. By extrapolating to the large- D limit, we obtain a final estimation $M_p = 0.1376$, which is a strong indication that the ground state breaks the Z_2 symmetry between two inequivalent squares. The convergence with respect to χ plotted in Fig. 10(b) indicates that the symmetry breaking is robust and is not a finite- χ effect. To show the detailed pattern and distinguish the two possible VBS states^{10,36}, we plot the bond correlation $\langle \mathbf{S}_i \cdot \mathbf{S}_j \rangle$ for each bond in Fig. 8(c). It shows that the correlation in squares without J' couplings is much stronger than that in squares with J' couplings, consistent with the empty-plaquette VBS state. Furthermore, we find the obtained ground state has a tiny magnetization of $\sim 10^{-4}$, suggesting it probably does not break the SU(2) spin symmetry. Combining these features, we can convincingly conclude that the ground state is an empty-plaquette VBS state at $J = 0.7$, consistent with previous studies¹⁰.

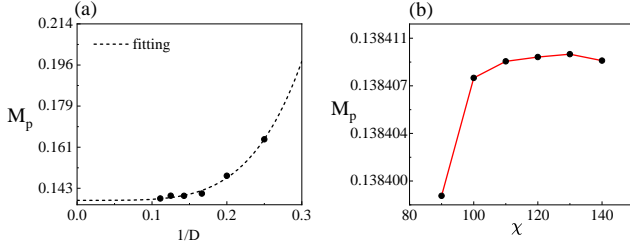


FIG. 10: The obtained order parameter M_p , defined in Eq. (12), of the Shastry-Sutherland model at $J = 0.7$. (a) M_p as a function of bond dimension D , with D ranging from 4 to 9. A power-law fitting of data $M_p(1/D)$ is also shown and denoted by a black dashed line. (b) The convergence analysis of $M_p(\chi)$ for $D = 9$.

For $J = 0.8$, we plot the ground-state energy in Fig. 11. The behavior is similar to that for $J = 0.7$, and the energy systematically lowers and gradually converges as D becomes larger. When $D = 9$, we have $E_g = -0.448708$. This is already very close to the previous tensor network studies, such as an infinite projected entangled simplex state (iPESS) study¹⁰, an infinite PEPS study employing U(1) spin symmetry⁵¹, and an extrapolation from finite PEPS calculation⁴⁷. These estimations are also included in Fig. 11 for comparison. Extrapolation to the large- D limit via a simple power-law fitting yields an estimate $E_g = -0.4490$, which is more reliable. With χ up to 160, Fig. 11 shows that the convergence precision of the ground-state energy for $D = 9$ has reached the order 10^{-6} , indicating the obtained result is convincing.

In Fig. 12, we plot the magnetization M of the obtained ground state as a function of D . It shows that though M becomes weaker and weaker as D increases, it remains finite and nonzero. For example, when $D = 9$, we still obtain a significant magnetization of about 0.1303, and an extrapolation in the large- D limit still

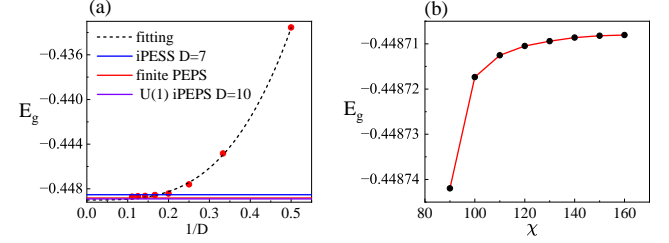


FIG. 11: The obtained ground-state energy E_g of the Shastry-Sutherland model at $J = 0.8$. (a) E_g as a function of bond dimension D , with D ranging from 2 to 9. A power-law fitting of data $E_g(1/D)$ is indicated by a black dashed line. For comparison, an iPESS study¹⁰, an infinite PEPS study employing U(1) symmetry⁵¹, and an extrapolation from finite PEPS calculations⁴⁷, are also included as solid lines. (b) The convergence analysis of $E_g(\chi)$ for $D = 9$.

gives a nonzero estimation of about $M = 0.12$. This is neither an artificial finite- χ effect, since by pushing χ to 160, the convergence precision of M for $D = 9$ has also reached the order 10^{-6} , as clearly shown in Fig. 12(b). This is unambiguously consistent with the fact that $J = 0.8$ falls in the antiferromagnetic phase.

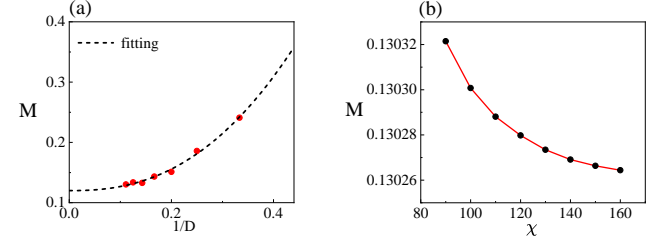


FIG. 12: The obtained order parameter M , defined in Eq. (10), of the Shastry-Sutherland model at $J = 0.8$. (a) M as a function of bond dimension D , with D ranging from 3 to 9. A power-law fitting to the data $M(1/D)$ is also shown in black dashed. (b) The convergence analysis of $M(\chi)$ for $D = 9$.

IV. DISCUSSIONS

In this work, we propose a single-layer framework that integrates the nested tensor network method into the variational tensor network calculations leveraging automatic differentiation. This framework can reduce the memory and computational costs by two and three orders of D compared to traditional variational calculations, thereby enabling D to be larger and achieving better accuracy. The validity of the framework is demonstrated through two prototypical models: the square lattice Heisenberg model and the Shastry-Sutherland model. Even without GPU hardware acceleration or symmetry

considerations, we can extend D to 9, yielding accurate ground-state energies and consistent order parameters with previous studies. Especially, for the Shastry-Sutherland model, we confirm an intermediate empty-plaquette VBS phase in the ground state diagram. The convergence with respect to D and χ is systematically analyzed, and nearly complete convergence is observed even for the largest D . We believe this framework could enable large-scale variational tensor network calculations in more complex quantum systems, such as superconductivity^{12,13}, excited states, and dynamical studies^{11,52} in the future.

In our calculations, the single-layer tensor network with nested structure is contracted by the CTMRG algorithm. It is known that the idea of nested tensor network can be performed not only in CTMRG^{40,41}, but also in other tensor contraction algorithms, such as time-evolving block decimation^{34,42,43}, and coarse-graining renormalization group. Therefore, correspondingly, the single-layer framework in this work can also be realized in other algorithms than CTMRG. The extra acceptable sacrifice is probably the same, i.e., the size of the unit cell of the single-layer nested tensor network may be doubled, as shown in Fig. 2(c) in this work.

The bond dimension D can be further increased by incorporating additional advanced techniques into this framework. For example, in this work we did not consider the spin symmetry, but one can leverage the U(1) symmetry of the two models to improve efficiency. For the square lattice Heisenberg model in this work, one can utilize a local spin rotation $-i\sigma_y$ on one set of lattice locations^{11,53} to reduce the 4×4 unit cell to a 2×2 unit cell in the generated nested tensor network, which can simplify the calculations shown in Fig. 2(c). Even for the Shastry-Sutherland model, this strategy can accelerate the convergence in variational calculations. Moreover, one can use a checkpoint²⁹ or a fixed-point technique to reduce the length of the chain, i.e., Eq. (5) used in

the back propagation, by calculating the gradient from a given or an approximate fixed-point environment⁵⁴. The latter strategy is similar to the finite-system approximation⁵⁵ or to choosing a better initial value for the CTMRG environment and can effectively reduce memory and computational costs in automatic differentiation calculations. Finally, at a purely computational level, one can use partial singular value decomposition, randomized decomposition⁵⁶ in Eq. (9), or employ a more economical QR decomposition⁵⁷ instead, to reduce computational cost further.

It is worth noting that several recent studies also involve single-layer tensor network states in the literature. For example, in Ref.⁵⁸, Jan *et al.* proposed a similar framework called the split-CTMRG algorithm, which is also based on the nested tensor network structure revealed in Ref.³⁴. However, the contraction scheme is designed particularly and differs from what we proposed in Sec. II C. In Ref.⁵⁹, Xu *et al.* extended the idea of nested structure to a triple-layer tensor network and applied it to the three-dimensional Ising model successfully, while earlier in Ref.⁶⁰, Yang *et al.* proposed a new nesting structure which is more natural and symmetric than the one proposed in Ref.³⁴ and was applied successfully to the same model. Probably, these single-layer proposals can be further improved by combining their distinct advantages, which we would like to leave as a future pursuit.

ACKNOWLEDGMENTS.

We are grateful to Prof. Tao Xiang and Ning Xi for helpful discussions, and to Jian-Gang Kong for reminding us of Ref.⁵⁸. This work was supported by the National R&D Program of China (Grants No. 2023YFA1406500 and No. 2024YFA1408604), the National Natural Science Foundation of China (Grants No. 12274458).

* qingtaoxie@ruc.edu.cn

¹ F. Verstraete, and J. I. Cirac, arXiv:cond-mat/0407066.

² R. Orus, Nat. Rev. Phys. **1**, 538 (2019)

³ Shi-Ju Ran, Emanuele Tirrito, Cheng Peng, Xi Chen, Luca Tagliacozzo, Gang Su, and Maciej Lewenstein, *Tensor Network Contractions*, Springer (Open, 2020).

⁴ R. Orus, Annals of Phys. **349**, 117 (2014).

⁵ Jorge Nocedal, Stephen J. Wright, *Numerical Optimization*, Springer (New York, 1999).

⁶ Tao Xiang, *Density Matrix and Tensor Network Renormalization*, Cambridge University Press (2023).

⁷ Simon Montangero, *Introduction to Tensor Network Methods*, Springer (Switzerland, 2018).

⁸ H. J. Liao, Z. Y. Xie, J. Chen, Z. Y. Liu, H. D. Xie, R. Z. Huang, B. Normand, T. Xiang, Phys. Rev. X **118**, 137202 (2017).

⁹ Wen-Yuan Liu, Didier Poilblanc, Shou-Shu Gong, Wei-Qiang Chen, Zheng-Cheng Gu, Phys. Rev. B **109**, 235116 (2024).

(2024).

¹⁰ Ning Xi, Hongyu Chen, Z. Y. Xie, Rong Yu, Phys. Rev. B **107**, L220408 (2023)

¹¹ Yang Liu, Shiqi Shao, Saisai He, Z. Y. Xie, Jia-Wei Mei, Hong-Gang Luo, and Jize Zhao, Phys. Rev. B **111**, 245117 (2025).

¹² Z. T. Xu, Z. C. Gu, and S. Yang, Phys. Rev. B **108**, 035144 (2023).

¹³ P. Corboz, Phys. Rev. B **93**, 045116 (2016).

¹⁴ P. Corboz, T. M. Rice, and M. Troyer, Phys. Rev. Lett. **113**, 046402 (2014).

¹⁵ Norbert Schuch, Didier Poilblanc, J. Ignacio Cirac, David Perez-Garcia, Phys. Rev. Lett. **111**, 090501 (2013).

¹⁶ Rui Wang, Tao Yang, Z. Y. Xie, Baigeng Wang, X. C. Xie, Phys. Rev. B **109**, L241113 (2024).

¹⁷ F. Verstraete, and J. I. Cirac, Phys. Rev. Lett. **104**, 190405 (2010).

¹⁸ Antoine Tilloy, and J. I. Cirac, Phys. Rev. X **9**, 021040 (2019).

¹⁹ M. Suzuki, Prog. Theor. Phys. **56**, 1454 (1976).

²⁰ Z. Y. Xie, J. Chen, M. P. Qin, J. W. Zhu, L. P. Yang, T. Xiang, Phys. Rev. B **86**, 045139 (2012).

²¹ H. C. Jiang, Z. Y. Weng, and T. Xiang, Phys. Rev. Lett. **101**, 090603 (2008)

²² Ling Wang, Frank Verstraete, arXiv:1110.4362.

²³ M. Lubasch, J. I. Cirac, and M. C. Banuls, Phys. Rev. B **90**, 064425 (2014).

²⁴ Ho N. Phien, Johann A. Bengua, Hoang D. Tuan, Philippe Corboz, Roman Orus, Phys. Rev. B **92**, 035142 (2015).

²⁵ Charles C. Margossian, arXiv:1811.05031.

²⁶ Ian Goodfellow, Yoshua Bengio, and Aaron Courville, *Deep Learning*, MIT Press (2016).

²⁷ The official website of PyTorch is at <https://pytorch.org>.

²⁸ The website of Zygote is at <https://fluxml.ai/Zygote.jl>.

²⁹ Hai-Jun Liao, Jin-Guo Liu, Lei Wang, and Tao Xiang, Phys. Rev. X **9**, 031041 (2019).

³⁰ N. Schuch, M. M. Wolf, F. Verstraete, J. I. Cirac, Phys. Rev. Lett. **98**, 140506 (2007).

³¹ T. Nishino and K. Okunishi, J. Phys. Soc. Jpn. **65**, 891 (1996).

³² R. Orus, and G. Vidal, Phys. Rev. B **80**, 094403 (2009).

³³ X. F. Liu, Y. F. Fu, W. Q. Yu, J. F. Yu, Z. Y. Xie, Chin. Phys. Lett. **39**, 067502 (2022).

³⁴ Z. Y. Xie, H. J. Liao, R. Z. Huang, H. D. Xie, J. Chen, Z. Y. Liu, and T. Xiang, Phys. Rev. B **96**, 045128 (2017).

³⁵ Anders W. Sandvik, AIP Conf. Proc. **1297**, 135 (2010)

³⁶ P. Corboz, and F. Mila, Phys. Rev. B **87**, 115144 (2013).

³⁷ D. E. Rumelhart, G. E. Hinton, and R. J. Williams, Nature **323**, 533–536 (1986).

³⁸ B. B. Chen, Y. Gao, Y. B. Guo, Y. Liu, H. H. Zhao, H. J. Liao, L. Wang, T. Xiang, W. Li, Z. Y. Xie, Phys. Rev. B **101**, 220409(R) (2020).

³⁹ Yang Liu, Z. Y. Xie, Hong-Gang Luo, Jize Zhao, Phys. Rev. B **107**, L041106 (2023).

⁴⁰ Chih-Yuan Lee, B. Normand, and Ying-Jer Kao, Phys. Rev. B **98**, 224414 (2018).

⁴¹ R. Haghshenas, Shou-Shu Gong, and D. N. Sheng, Phys. Rev. B **99**, 174423 (2019).

⁴² G. Vidal, Phys. Rev. Lett. **98**, 070201 (2007).

⁴³ R. Orus, and G. Vidal, Phys. Rev. B **78**, 155117 (2008).

⁴⁴ In principle, the dimension of each bond can be different. For example, in the case of Fig. 2(c), all the bonds have dimension D except the left and down bonds of tensor Y , which are of dimension Dd . In the main text, we assume all the bonds have the same dimension just for simplicity of description. In the meantime, since d is almost always much smaller than D , we ignore the scaling of d when the computational cost and the memory cost are considered in the main text.

⁴⁵ P. Corboz, Phys. Rev. B **94**, 035133 (2016).

⁴⁶ P. Corboz, and F. Mila, Phys. Rev. Lett. **112**, 147203 (2014).

⁴⁷ Wen-Yuan Liu, Xiao-Tian Zhang, Zhe Wang, Shou-Shu Gong, Wei-Qiang Chen and Zheng-Cheng Gu, Phys. Rev. Lett. **133**, 026502 (2024).

⁴⁸ T. Senthil, A. Vishwanath, L. Balents, S. Sachdev, and M. P. A. Fisher, Science **303**, 1490–1494 (2004).

⁴⁹ Y. Cui, L. Liu, H. Lin, K.-H. Wu, W. Hong, X. Liu, C. Li, Z. Hu, N. Xi, S. Li, R. Yu, A. W. Sandvik, and W. Yu, Science **380**, 1179 (2023).

⁵⁰ Jianwei Yang, Anders W. Sandvik, and Ling Wang, Phys. Rev. B **105**, L060409 (2022).

⁵¹ Philippe Corboz, Yining Zhang, Boris Ponsioen, and Frederic Mila arXiv:2502.14091.

⁵² Boris Ponsioen, Fakher F. Assaad, and P. Corboz, SciPost Phys. **12**, 006 (2022).

⁵³ J. Hasik, D. Poilblanc, and F. Becca, SciPost Phys. **10**, 012 (2021).

⁵⁴ Hao Xie, Jin-Guo Liu, Lei Wang, Phys. Rev. B **101**, 245139 (2020).

⁵⁵ H. H. Zhao, Z. Y. Xie, Q. N. Chen, Z. C. Wei, J. W. Cai, T. Xiang, Phys. Rev. B **81**, 174411 (2010).

⁵⁶ S. Morita, R. Igarashi, Hui-Hai Zhao, and Naoki Kawashima, Phys. Rev. E **97**, 033310 (2018).

⁵⁷ Yining Zhang, Qi Yang, Philippe Corboz, arXiv:2505.00494.

⁵⁸ Jan Naumann, Erik Lennart Weerda, Jens Eisert, Matteo Rizzi, Philipp Schmoll, Phys. Rev. B **111**, 235116 (2025).

⁵⁹ Xia-Ze Xu, Tong-Yu Lin, Guang-Ming Zhang, Phys. Rev. B **112**, 134403 (2025).

⁶⁰ Li-Ping Yang, Y. F. Fu, Z. Y. Xie, T. Xiang, Phys. Rev. B **107**, 165127 (2023).